# Single-molecule analysis reveals the phosphorylation of FLS2 governs its spatiotemporal dynamics and immunity

Yaning Cui[1,2,5], Hongping Qian[2,5], Jinhuan Yin[2], Changwen Xu[2], Pengyun Luo[2], Xi Zhang[2], Meng Yu[3], Bodan Su[4], Xiaojuan Li[2], Jinxing Lin[1,2*]

[1]State Key Laboratory of Tree Genetics and Breeding, College of Biological Sciences and Technology, Beijing Forestry University, Beijing 100083, China;
[2]National Engineering Research Center of Tree Breeding and Ecological Restoration, College of Biological Sciences and Technology, Beijing Forestry University, Beijing 100083, China
[3] College of Life Sciences, Hebei Agricultural University, Baoding, 071001, China
[4] Biotechnology Research Institute, Beijing 100081, China
[5] These authors contributed equally
[*]Correspondence: Jinxing Lin (linjx@ibcas.ac.cn)

## Summary

The *Arabidopsis thaliana* FLAGELLIN-SENSITIVE2 (FLS2), a typical receptor kinase, recognizes the conserved 22 amino acid sequence in the N-terminal region of flagellin (flg22) to initiate plant defense pathways, which was intensively studied in the past decades. However, the dynamic regulation of FLS2 phosphorylation at the plasma membrane after flg22 recognition needs further elucidation. Through single-particle tracking, we demonstrated that upon flg22 treatment, the phosphorylation of Ser-938 in FLS2 impacts its spatiotemporal dynamics and lifetime. Following förster resonance energy transfer-fluorescence lifetime (FRET-FLIM) imaging microscopy and protein proximity indexes (PPI) assays revealed that flg22 treatment increased the co-localization of GFP-tagged FLS2/FLS2$^{S938D}$ but not FLS2$^{S938A}$ with AtRem1.3-mCherry, a sterol-rich lipid marker, indicating that the phosphorylation of FLS2$^{S938}$ affects FLS2 sorting efficiency to AtRem1.3-associated nanodomains. Importantly, we found that the phosphorylation of Ser-938 enhanced flg22-induced FLS2 internalization and immune responses, demonstrating that the phosphorylation may activate

flg22-triggered immunity through partitioning FLS2 into functional *At*Rem1.3-associated nanodomains, which fills the gap between the FLS2$^{S938}$ phosphorylation and FLS2-mediated immunity.

**Keywords:** single-molecule analysis; phosphorylation; spatiotemporal dynamics; *At*Rem1.3-associated nanodomains; endocytosis; immunity;

## Introduction

Plasma-membrane (PM) localized receptor kinase (RK) plays a crucial role in pattern-triggered immunity (PTI), the initial defense layer in plants, features with an extracellular domain, a single transmembrane region, and a cytoplasmic kinase domain (Liang et al., 2018). FLAGELLIN-SENSING 2 (FLS2), a star RK in PTI, senses a conserved N-terminal epitope (flg22) of the bacterial flagellin (Hudson et al., 2024). Upon flg22 perception, FLS2 rapidly interacts with its co-receptor brassinosteroid insensitive1-associated kinase1 (BAK1) to form an active receptor complex (Chinchilla et al., 2006; Chinchilla et al., 2007; Heese et al., 2007), initiating phosphorylation events through activating receptor-like cytoplasmic kinases (RLCKs) such as BOTRYTIS-INDUCED KINASE 1 (BIK1) to elicit downstream immune responses (Lu et al., 2010; Zhang et al., 2010).

Protein phosphorylation, a vital post-translational modification, plays an essential role in signal transduction. Previous studies suggest that protein phosphorylation alterations affect protein dynamics and subcellular trafficking (Kaiserli et al., 2009; Kontaxi et al., 2023). In plants, phosphorylation of proteins can coalesce into membrane nanodomains, forming platforms for active protein function at the PM (Bücherl et al., 2017). For example, Xue et al. (2018) demonstrated that phosphorylation of the blue light receptor phot1 accelerates the protein movement, enhancing its interaction with a sterol-rich lipid marker *At*Rem1.3-mCherry, which underscores the crucial role of protein phosphorylation in protein dynamics and membrane partitioning. Upon flg22

treatment, multiple FLS2 phosphorylation sites are activated, with the Serine-938 phosphorylation playing a pivotal role in defense activation (Cao et al., 2013); nevertheless, how the phosphorylation of FLS2$^{S938}$ impacts on plant immunity remains elusive.

Membrane nanodomains, which are crucial in regulating PM protein behavior, are dynamic structures enriched with sterols and sphingolipids (Boutté et al., 2020) and uniquely labeled by proteins such as Flotillins and Remorins within living cells (Martinière et al., 2021). Various stimuli are able to trigger PM proteins moving into mobile or immobile nanodomains, suggesting a connection between nanodomains and signal transduction (Wang et al., 2015). For example, Xing et al. (2022) demonstrated that sterol depletion significantly impacts the dynamics of flg22-activated FER-GFP, emphasizing the role of nanodomains in the lateral mobility and dissociation of FER from the PM under flg22 treatment. However, the spatial coordination of FLS2 dynamics and signaling at the PM, and their relationships with nanodomains remain poorly understood.

To investigate whether the FLS2$^{S938}$ phosphorylation activates immune responses through nanodomains, we analyzed the diffusion and lifetime of FLS2 phospho-dead and phospho-mimic mutants at the PM before and after flg22 treatments. Our results show that flg22-induced dynamic and lifetime changes were abolished in FLS2$^{S938A}$. Using FLIM-FRET and smPPI techniques, we found that FLS2 phosphorylation variants exhibited distinct membrane nanodomain distribution and endocytosis. Importantly, we demonstrated that the immune response of phosphor-mimic FLS2$^{S938D}$ was comparable to wild-type FLS2, while the phosphor-dead version of FLS2$^{S938A}$ weakened the immune response. Our findings pinpoint the missing piece of FLS2-mediated immune signaling *in planta.*

## Results and Discussion

### The Ser-938 phosphorylation site changed the spatiotemporal dynamics of flg22-induced FLS2 at the plasma membrane

Previous studies highlight the crucial role of membrane protein phosphorylation in fundamental cellular processes, including PM dynamics (Vitrac et al., 2019; Offringa et al., 2013). *In vitro* mass spectrometry (MS) identified multiple phosphorylation sites in FLS2. Genetic analysis further identified Ser-938 as a functionally important site for FLS2 *in vivo* (Cao et al., 2013). FLS2 Ser-938 mutations impact flg22-induced signaling, while BAK1 binding remains unaffected, thereby suggesting Ser-938 regulates other aspects of FLS2 activity (Cao et al., 2013). To unravel the immune response regulation mechanisms via FLS2 phosphorylation, we generated transgenic Arabidopsis plants expressing C-terminal GFP-fused FLS2, S938A, or S938D under the FLS2 native promoter in the *fls2* mutant background (Figure S1A). Using VA-TIRFM with single-particle tracking (Figure 1A and 1B), we investigated the diffusion dynamics of FLS2 phospho-dead and phospho-mimic mutants, following previous reports (Geng et al., 2022). Upon flg22 treatment, FLS2/FLS2$^{S938D}$-GFP spots demonstrated extended motion trajectories, contrasting with the shorter motion tracks of FLS2$^{S938A}$-GFP spots (Figure 1C). The results indicate significant changes in the diffusion coefficients and motion ranges of FLS2/FLS2$^{S938D}$-GFP after flg22 treatment, whereas FLS2$^{S938A}$-GFP showed no significant differences (Figure 1D and 1E). Similar results were obtained using Uniform Manifold Approximation and Projection (UMAP) technology (Dorrity et al., 2020) (Figure 1F and S1B) and fluorescence recovery after photobleaching (FRAP) (Greig et al., 2021) (Figure 1G, H and S1C), supporting the essential role of the S938 phosphorylation site in flg22-induced lateral diffusion of FLS2 at the PM.

Using VA-TIRFM, we analyzed FLS2 particle lifetime across various phosphorylation states. The results revealed that flg22 treatment significantly

reduced the fluorescence trajectory of FLS2 molecules compared to the control (Figure S1D), indicating that Ser-938 phosphorylation influences flg22-induced lifetime of FLS2 at the PM. Subsequently, real-time dynamic analysis through the Kymograph technique provided spatiotemporal information via frame-by-frame tracking (Zhou et al., 2020; Su et al., 2023). Compared to FLS2-GFP and FLS2$^{S938D}$-GFP, FLS2$^{S938A}$-GFP showed nearly linear fluctuations in fluorescence intensity under flg22 conditions, and the duration of fluorescence retention was essentially unchanged (Figure S1E). To validate this, we used an exposure time of 100 ms to capture a time series with a total duration of 20 s. Therefore, we divided the times into three segments: 0-1s, 1-4s, and >4s (Bücherl et al. 2017). Numerous FLS2 molecules exhibited a short-lived lifetime, which could be attributed to fluorescence bleaching or potentially reflect the occurrence of abortive endocytic events (Bertot et al., 2018). Additionally, we focused on lifetimes exceeding 4 s. The results showed after flg22 treatment, the lifetime of FLS2$^{S938D}$-GFP greater than 4S significantly decreased, resembling that of FLS2-GFP. While FLS2$^{S938A}$-GFP plants showed a minor decrease in lifetime upon flg22 treatment, this change was insignificant (Figure 1I and S1F). This aligns with previous findings that indicated that NRT1.1 phosphorylation affects dynamics and lifetime (Zhang et al., 2019). Therefore, these results underscore the impact of Ser-938 phosphorylation on the spatiotemporal dynamics of flg22-induced FLS2.

**Ser-938 phosphorylation enhances recruitment of FLS2/BAK1 heterodimerization into *At*Rem1.3-associated nanodomains**

Proteins rarely act independently; they typically form multimers to enhance downstream signaling (Li et al., 2022). Flg22 treatment induces FLS2 and BAK1 to heterodimerize at the PM, signifying flg22 as a ligand promoting this heterodimerization (Orosa et al., 2018). To investigate the impact of Ser-938 phosphorylation on FLS2/BAK1 heterodimerization, we employed Tesseler technology, analyzing FLS2 and BAK1 colocalization in *N.*

*benthamiana* epidermal cells. Partial colocalization of FLS2-GFP, FLS2$^{S938A}$-GFP, and FLS2$^{S938D}$-GFP with BAK1-mCherry was observed after treatment (Figure S2A), suggesting that heterodimerization formation is independent of Ser-938 phosphorylation. To further verify if FLS2/BAK1 heterodimerization requires Ser-938 phosphorylation, we analyzed the donor fluorescence lifetime (t) and corrected fluorescence resonance energy transfer (FRET) efficiency (IPS value). A significant decrease in GFP lifetime (t) was observed in leaves expressing FLS2/FLS2$^{S938D}$/FLS2$^{S938A}$ and BAK1-mCherry upon flg22 application (Figure 2A). The FRET efficiency (IPS) between FLS2, FLS2$^{S938D}$, and FLS2$^{S938A}$ with BAK1-mCherry significantly increased after flg22 treatment, suggesting that the FLS2 Ser-938 phosphorylation site is not essential for flg22-induced heterodimerization. To validate this observation, we quantified FLS2/FLS2$^{S938D}$/FLS2$^{S938A}$ and BAK1-mCherry colocalization using Pearson correlation coefficients. A marked increase in the coefficient after flg22 treatment for FLS2/FLS2$^{S938D}$/FLS2$^{S938A}$ and BAK1-mCherry (Figure 2B and S2B) indicated flg22-induced interaction between FLS2-GFP and BAK1-mCherry, irrespective of FLS2 Ser-938 phosphorylation. Additionally, we applied protein proximity indexes to estimate the degree of co-localization between FLS2/FLS2$^{S938D}$/FLS2$^{S938A}$ and BAK1-mCherry. After flg22 treatment, mean protein proximity indexes of FLS2, FLS2$^{S938D}$, and FLS2$^{S938A}$ with BAK1 increased (Figure 2C and S2C), thereby further supporting our findings. This aligns with the previous finding that flg22 acts as a molecular glue for FLS2 and BAK1 ectodomains (Sun et al., 2013), confirming the independence of FLS2/BAK1 heterodimerization from phosphorylation, with these events occurring sequentially.

Membrane nanodomains serve as pivotal platforms for protein regulation, impacting cellular signaling dynamics (Martinière et al., 2021). Studies reveal that specific plasma membrane (PM) proteins, responsive to developmental cues and environmental stimuli, exhibit dynamic movements within and

outside these nanodomains (Lee et al., 2019). For instance, treatment with the secreted peptides RAPID ALKALINIZATION FACTOR (RALF1 and RALF23) enhances the presence of FERONIA (FER) in membrane nanodomains (Gronnier et al., 2022). Conversely, flg22-activated BSK1 translocates from membrane nanodomains to non-membrane nanodomains (Su et al., 2021). In a previous investigation, we demonstrated that flg22 induces FLS2 translocation from AtFlot1-negative to AtFlot1-positive nanodomains in the plasma membrane, implying a connection between FLS2 phosphorylation and membrane nanodomain distribution (Cui et al., 2018). To validate this, we assessed the association of FLS2/FLS2$^{S938D}$/FLS2$^{S938A}$ with membrane nanodomains, using *At*Rem1.3-associated nanodomains as representatives (Lv et al., 2017; Huang et al., 2019). Upon observation using dual-color TIRM-SIM, partial co-localization was detected between FLS2-GFP, FLS2$^{S938D}$-GFP, FLS2$^{S938A}$-GFP, and *At*Rem1.3-mCherry foci on cell surfaces (Figure 2D). Single particle tracking (SPT) was employed to quantify the colocalization ratio, revealing a small overlap in the cross-correlation signal for FLS2$^{S938A}$-GFP and *At*Rem1.3-mCherry after flg22 treatment, similar to untreated cells. In contrast, flg22-treated seedlings displayed higher cross-correlation signals for FLS2-GFP/FLS2$^{S938D}$-GFP and *At*Rem1.3-mCherry compared to untreated seedlings (Figure 2E and F), suggesting that phosphorylation increased the movement of FLS2 protein to membrane nanodomains. To further verify this result, FRET-FLIM was applied to examine the correlation between FLS2/FLS2$^{S938D}$/FLS2$^{S938A}$-GFP and *At*Rem1.3-mCherry. The results showed that, after flg22 treatment, plants co-expressing FLS2$^{S938D}$-GFP with *At*Rem1.3-mCherry had a strongly reduced average GFP fluorescence lifetime compared to control seedlings, which was similar to that of FLS2-GFP seedlings (Figure 2G, H). Meanwhile, the flg22 treatment increased the IPS for FLS2 and FLS2$^{S938D}$ with *At*Rem1.3-mCherry. No significant difference was observed in the fluorescence lifetime and IPS of FLS2$^{S938A}$-GFP co-expressed with AtRem1.3-mCherry, with or without flg22

treatment (Figure 2G, H), suggesting that Ser-938 phosphorylation may influence FLS2 partitioning into PM nanodomains. To further investigate the role of phosphorylation in FLS2 distribution into nanodomains, we used Pearson's correlation coefficients to quantify the co-localization between FLS2/FLS2$^{S938D}$/FLS2$^{S938A}$-GFP and *At*Rem1.3-mCherry. It was found that the mean co-localization values between FLS2-GFP/FLS2$^{S938D}$-GFP and *At*Rem1.3-mCherry under flg22 treatment were significantly higher compared to control group (Figure 2I). Notably, FLS2$^{S938A}$-GFP and *At*Rem1.3-mCherry demonstrated similar co-localization values under both control group and flg22 conditions (Figure 2I), indicating that the phosphorylated form of FLS2 may modify the distribution of PM nanodomains. These findings suggest that the phosphorylation state of FLS2 at Ser-938 influences its aggregation into *At*Rem1.3-associated nanodomains, providing an efficient mechanism for triggering the immune response.

**Ser-938 phosphorylation maintains FLS2 protein homeostasis via flg22-induced endocytosis**

The PM protein endocytosis is crucial for regulating intercellular signal transduction in response to environmental stimuli. Notably, Thr 867 mutation, a potential phosphorylation site on FLS2, results in impaired flg22-induced endocytosis, underscoring the significance of phosphorylation in FLS2 endocytosis (Robatzek et al., 2006). As shown in Figure 1I, both FLS2 and FLS2 phospho-mimetic mutants showed a reduced lifetime under flg22 treatment, implying a probable connection between FLS2 lifetime and endocytosis. We further found that FLS2/FLS2$^{S938D}$/FLS2$^{S938A}$-GFP accumulated in BFA compartments labeled with FM4-64, indicating that various Ser-938 phosphorylation states of FLS2 undergo BFA-dependent constitutive endocytosis (Figure 3A, S3A).

Next, we investigated the impact of Ser-938 on flg22-induced FLS2 internalization. Under co-treatment with BFA and flg22, FLS2/FLS2$^{S938D}$

233 produced strong signals in both the BFA compartments. Interestingly, we
234 found that FLS2$^{S938A}$-GFP only produced BFA compartments, and most
235 remained at the PM region with few intracellular puncta upon stimulation with
236 BFA and flg22, (Figure S3B-E). We further tracked FLS2 endocytosis and
237 quantified vesicle numbers over time, the results showed that both FLS2 and
238 FLS2$^{S938D}$ vesicles appeared 15 min after-flg22 treatment, significantly
239 increasing thereafter. Notably, only a few vesicles were detected in
240 FLS2$^{S938A}$-GFP, indicating Ser-938 phosphorylation of FLS2 impact on
241 flg22-induced FLS2 endocytosis (Figure 3B, C and S3F). Results revealed
242 increased endocytic vesicles for FLS2 during flg22 treatment, aligning with
243 previous studies (Leslie et al., 2017; Loiseau et al., 2017). Additionally,
244 fluorescence correlation spectroscopy (FCS) (Chen et al., 2009) monitored
245 molecular density of FLS2 changes on the PM before and after flg22 treatment
246 (Figure S3G). Figure 3D shows that both FLS2-GFP and FLS2$^{S938D}$-GFP
247 densities significantly decreased after flg22 treatment, while FLS2$^{S938A}$-GFP
248 exhibited minimal changes, indicating Ser-938 phosphorylation affects FLS2
249 internalization. Western blotting confirmed that Ser-938 phosphorylation
250 influences FLS2 degradation after flg22 treatment (Figure 3E), consistent with
251 single-molecule analysis findings. Therefore, our results strongly support the
252 notion that Ser-938 phosphorylation expedited FLS2 internalization, potentially
253 regulating its immune response capacity.

254 **Ser-938 Phosphorylation affects FLS2-mediated responses**

255 PTI plays a pivotal role in host defense against pathogenic infections
256 (Macho and Zipfel, 2014; Ding et al., 2022; Ngou et al., 2022). Previous
257 studies demonstrated that the perception of flg22 by FLS2 initiates a complex
258 signaling network with multiple parallel branches, including calcium burst,
259 mitogen-activated protein kinases (MAPKs) activation, callose deposition, and
260 seedling growth inhibition (Chi et al., 2021; Zipfel et al., 2004; Li et al., 2016;
261 Sanguankiattichai et al., 2022). Our focus was to investigate the significance of

Ser-938 phosphorylation in flg22-induced plant immunity. Our results illustrates diverse immune responses in FLS2 and FLS2$^{S938D}$ plants following flg22 treatment (Figure 4A-F, S4). These responses encompass calcium burst activation, MAPKs cascade reaction, callose deposition, hypocotyl growth inhibition, and activation of immune-responsive genes. In contrast, FLS2$^{S938A}$ exhibited limited immune responses, underscoring the importance of Ser-938 phosphorylation for FLS2-mediated PTI responses.

In summary, our study confirmed that FLS2 phosphorylation regulated PAMP-triggered plant immunity by influencing spatiotemporal dynamics at the PM. Following flg22 treatment, activated FLS2 undergoes hetero-oligomerization and phosphorylation sequentially (Figure 4 G and H). Crucially, phosphorylation at the Ser-938 site promotes FLS2 recruitment into *At*Rem1.3-associated nanodomains and endocytosis (Figure 4 G and H). These results provided new insights into the phosphorylation-regulated dynamics of plant immunity, thereby providing a reference for future studies on signal transduction in intracellular complex nanostructures.

## Acknowledgments

This work was supported by the National Natural Science Foundation of China (32030010, 91954202, 32370740, 32000483, 32170689), the Fundamental Research Funds for the Central Universities (NO.QNTD202301), National Key Research and Development Program of China (2022YFF0712500, 2022YFD2200603), Beijing Nova Program (20230484251), 5·5 Engineering Research & Innovation Team Project of Beijing Forestry University (BLRC2023C06).

## Author contributions

J.L., Y.C. and X.L. designed the research; Y.C., H.Q., C.X. and J.Y. performed the research; C.X., P.L. and M.Y. contributed new reagents/analytic tools; X.Z., H.Q. and B.S. analyzed the data; and Y.C., H.Q. and J.L. wrote the paper.

## Declaration of interests

**(A)** The authors declare no competing interests.

## STAR Methods

### Plant Materials and Construction

Mutants and transgenic lines used in all experiments were in the *Arabadopsis thaliana* Colombia-0 (Col-0) background. To generate the transgenic plants, specific constructs were PCR-amplified and cloned into the vector pCAMBIA2300. Plasmids were introduced into the mutant plants by *Agrobacterium*-mediated transformation. Dual-color lines expressing $FLS2^{S938A}$-GFP and $FLS2^{S938D}$-GFP with REM1.3-mCherry were generated by hybridization.

### Transient infiltration of N. benthamiana leaves

The Agrobacterium tumefaciens strains GV3101 (obtained from Shanghai Weidi Biotechnology), harboring eukaryotic expression vectors, were infiltrated into the leaves of 8-week-old *N. benthamiana* plants. Plants were incubated at 22°C for 2 days before imaging.

## Drug Treatments

All chemicals were obtained from Sigma-Aldrich, and dissolved in 100% DMSO to yield stock solutions at the following concentrations: BFA (50 mM in DMSO, 50 μM in working solution), CHX (50 mM in DMSO, 50 μM in working solution), and FM4-64 (5 mM in DMSO, 5 μM in working solution). The flg22 of flagellin peptides was synthesized by Shanghai GL Biochem Company, and was used in a concentration of 10 μM in double-distilled H2O. *Arabidopsis* seedlings were treated in 1/2 MS growth liquid medium with added hormone or drug.

## Quantitative Reverse-transcription PCR

Total RNA was extracted using the Plant Kit (Tiangen), and then reverse transcribed into cDNA with FastQuant RT Kit (Tiangen). Next, qPCR was performed using TiangenSurperRealPreMix Plus (SYBR Geen). The primers used were as follows: WRKY33 (At At2g38470) 5′-GAAACAAATGGTGGGAATGG-3′ and 5′-TGTCGTGTGATGCTCTCTCC-3′; CYP81 (At At2g23190) 5′-AAATGGAGAGAGCAACACAATG-3′ and 5′-ATCGCCCATTCCAATGTTAC-3′; FRK1 (AtAt2g19190) 5′-TATATGGACACCGCGTATAGTG-3′and 5′-ATAAAACTTTGCGTTAGGGTCG-3′.

## Aniline Blue Staining

To detect callose deposition, aniline blue staining was performed as described. *Arabidopsis thaliana* leaves were completely de-colored by the destaining solution (3 mL ethyl alcohol and 1 ml glacial acetic acid), rinsed in water and 50% ethanol, and then stained in 150 mM $KH_2PO_4$ (pH 9.5) plus 0.01% aniline blue for 2 h. Samples were mounted in 25% glycerol, and then observed under a microscope that was equipped with a Leica DM2500 UV lamp.

## Confocal Laser Scanning Microscopy and Image Analysis

Confocal microscopy was done with a TCS SP5 Confocal Microscope fitted with a 63X water-immersion objective. GFP and FM4-64 were assayed using

488-nm and 514-nm wavelengths (multitrack mode). The fluorescence emissions were respectively detected with spectral detector set LP 560–640 (FM4-64) and BP 520–555 (GFP). Image analysis was performed with Leica TCS SP5 software and quantified using the ImageJ software bundle (NIH).

**VA-TIRFM and Single-Particle Fluorescence Image Analysis**

The dynamics of FLS2 phospho-dead and phospho-mimic mutants were recorded using VA-TIRFM. This was done using an inverted microscope (IX-71, Olympus) equipped with a total internal reflective fluorescence illuminator (model no. IX2-RFAEVA-2; Olympus) and a 1003 oil-immersion objective (numerical aperture = 1.45). To track GFP-labeled proteins at the PM, living leaf epidermal cells of 6-day-old seedlings were observed under VA-TIRFM. To visualize GFP or mCherry fluorescent proteins, appropriate corresponding laser excitation (473-nm or 561-nm) was used and emission fluorescence was obtained with filters (BA510IF for GFP; HQ525/50 for mCherry). A digital EMCCD camera (Andor Technology, ANDOR iXon DV8897D-CS0-VP, Belfast, UK) was used to acquire the fluorescent signals, which were stored directly on computers and then analyzed with Image J software. Images of single particles were acquired with 100-ms exposure time.

**UMAP analysis**

We used an R package to perform dimensionality reduction and clustering analysis of single-particle tracking data. We performed nonlinear dimensionality reduction for visualization with the function "UMAP" in the R package. We proceeded to cluster cells using the Louvain algorithm with the "FindNeighbors" and "FindClusters" functions in the R package carried out as previously described (Dorrity et al., 2020).

**TIRF-SIM imaging and the colocalization analysis**

The SIM images were taken by a 60 × NA 1.49 objective on a structured illumination microscopy (SIM) platform (DeltaVision OMX SR) with a sCMOS camera (Camera pixel size, 6.5 μm). The light source for TIRF-SIM included

diode laser at 488 nm and 568 nm with pixel sizes (μm) of 0.0794 and 0.0794 (Barbieri et al., 2021).

For the dual-color imaging, FLS2/FLS2$^{S938A}$/FLS2$^{S938D}$-GFP (488 nm/30.0%) and AtRem1.3-mCherry (561 nm/30.0%) were excited sequentially. The exposure time of the camera was set at 50 ms throughout single-particle imaging. The time interval for time-lapse imaging was 100 ms, the total time was 2s, and the total time points were 21s. The Imaris intensity correlation analysis plugin was used to calculate the co-localization ratio as described previously. The sizes of the ROIs used for statistical analysis are 13.38 μm and 13.38 μm.

**$Ca^{2+}$ Flux Measurements in Arabidopsis Leaves**

Net $Ca^{2+}$ fluxes in Arabidopsis leaf cells were measured using the non-invasive micro-test technique (NMT), as described previously (Zhong et al., 2023). First, a small incision was made in the leaves of fourteen-day-old seedling. Then it was fixed at the bottom of 35 mm petri dish, and incubated in the test buffer( pH =6.0, 0.1 mmol $L^{-1}$KCl/$CaCl_2$/$MgCl_2$, 0.2 mmol $L^{-1}$ $Na_2SO_4$, 0.3 mmol $L^{-1}$ MES, 0.5 mmol $L^{-1}$ NaCl) for approximately 30 min. The $Ca^{2+}$ concentration in the leaf cells was measured at 0.2 Hz near and 30 μm away from the cells. Each plant was measured once, and then use 1/2 MS (CK) or 10 μM flg22 treated the leaf and measured $Ca^{2+}$flux again. The $Ca^{2+}$ flux was calculated as described (Jiao et al., 2022).

**Analysis of Root Growth**

The transgenic seedlings were treated with different conditions, and imaging was performed by scanning the root systems at 500 dpi (Canon EOS 600D). ImageJ was used to analyze the root growth parameters. Three biological replicates were performed.

**Fluorescence recovery after photobleaching analysis**

Plants were grown on ½MS solid medium for 4 days prior to conducting

fluorescence recovery after photobleaching (FRAP) analysis. The FRAP analysis was carried out using an Olympus FV1200 confocal microscope with an inverted microscope setup. The imaging was performed using 488-nm diode laser excitation and a water-immersed 63× objective. The area of interest was bleached with a 488 nm laser at 100% laser power. The time interval for monitoring fluorescence recovery was 3 seconds. The fluorescence recovery data was subsequently analyzed using ImageJ and Origin 8.6 software following the methods outlined by Xing et al. (2022).

**FCS**

FCS was performed in point-scanning mode on a Leica TCS SP5 FCS microscope equipped with a 488-nm argon laser, an Avalanche photodiode, and an in-house coupled correlator. After acquiring images on the PM of a cell in transmitted light mode, the diffusion of protein molecules into and out of the focal volume transformed the local concentration of fluorophores, leading to spontaneous fluctuation in the fluorescence intensity. Finally, the protein density was calculated on the basis of the protocol described previously.

**FRET-FLIM**

FRET-FLIM analysis was performed using an inverted Olympus FV1200 microscope equipped with a Picoquant picoHarp300 controller. The excitation at 488 nm was implemented by a picosecond pulsed diode laser at a reduplication rate of 40 MHz, by way of a water immersion objective (603, numerical aperture [NA] 1.2). The emitted light passed through a 520/35 nm bandpass filter and was detected by an MPD SPAD detector. Data were collected and performed using the SymphoTime 64 software (PicoQuant).

**Western Blot**

Total proteins were extracted from 10-day-old seedlings of the acidic phosphomimic mutants FLS2$^{S938A}$-GFP and FLS2$^{S938D}$-GFP and transgenic FLS2-GFP lines under different conditions. Proteins were extracted using buffer E [includes 1.5125 g Tris-HCl (pH 8.8), 1.2409 g $Na_2S_2O_5$, 11.1 ml

421 glycerine, 1 g SDS, and 5 mM DTT]. The proteins in PM fractions were
422 obtained using the Invent Minute kit. Proteins were separated by 10%
423 SDS-polyacrylamide gel and transferred to a nitrocellulose membrane. The
424 membrane was blotted with anti-GFP antibody (Sigma-Aldrich) at a 1:4000
425 dilution.

426 **SR-Tesseler**

427 The association of FLS2/FLS2$^{S938D}$/FLS2$^{S938A}$ with AtRem1.3-associated
428 nanodomains was characterized using the open-source software packages
429 ImageJ and SR-Tesseler. The specific operational steps were as previously
430 described (Levet et al., 2015).

431 **Protein proximity indexes (PPI) analysis**

432 The degree of correlation between proteins was analyzed by measuring the
433 protein proximity indexes (PPI) (Zinchuk et al., 2011). Recently, a
434 single-molecule protein proximity index (smPPI) was developed. Using
435 single-molecule images acquired via VA-TIRFM, the smPPI can be calculated
436 to quantitatively assess the colocalization of FLS2/FLS2$^{S938D}$/FLS2$^{S938A}$ with
437 AtRem1.3.

438 **Kymograph analysis**

439 The original images were uploaded to ImageJ, which includes the “multiple
440 kymograph” plugin. The image can be adjusted for optimum contrast by
441 selecting “Image/Adjustment/Brightness/Contrast”. Subsequently, the
442 individual particles of interest are selected using the “straight line” tool, and the
443 dynamic features are analyzed using the “Multiple Kymograph” tool. Finally,
444 the “Image/Type/RGB color” tool is utilized to obtain typical images, which are
445 then saved in TIFF format.

446 **Pearson analysis**

447 The co-localization analysis for FLS2/FLS2$^{S938D}$/FLS2$^{S938A}$ with
448 AtRem1.3/BAK1 was carried out using ImageJ as described previously (Zhang

et al., 2019). The background subtraction was performed using the 'Rolling Ball' method with a radius of 50 pixels. The plugin “PSC co-localization” in ImageJ was employed to derive the pearson correlation coefficient (Rr).

## Data analysis

The significance of arithmetic mean values for all data sets was assessed using Student’s t-test. Error bars were calculated with the s.d. function in Microsoft Excel. The differences at $P<0.05$ were considered statistically significant. According to Student’s t-test, characters in the figure represent statistically significant differences compared with control (**P<0.05, **P<0.01 and ***P<0.001*).

## Supplemental data

**Supplemental Figure S1.** Different Ser-938 phosphorylation states lead to specific spatiotemporal dynamics of FLS2.

**Supplemental Figure S2.** Different Ser-938 phosphorylation states do not affect the hetero-oligomerization of FLS2/BAK1.

**Supplemental Figure S3.** Effects of Ser-938 phosphorylation on the endocytosis of FLS2.

**Supplemental Figure S4.** Ser-938 phosphorylation affects flg22-induced PTI responses.

**Supplemental Movies 1-3.** TIRF-SIM movies of FLS2 (WT, A, D) and *At*Rem1.3-mCherry.

## References


Barbieri L, Colin-York H, Korobchevskaya K, Li D, Wolfson DL, Karedla N, Schneider F, Ahluwalia BS, Seternes T, Dalmo RA, Dustin ML, Li D, Fritzsche M. 2021. Two-dimensional TIRF-SIM-traction force microscopy (2D TIRF-SIM-TFM). *Nature Communications* **12**: 2169. DOI: 10.1038/s41467-021-22377-9. PMID: 33846317

Bertot L, Grassart A, Lagache T, Nardi G, Basquin C, Olivo-Marin J, Sauvonnet N. 2018. Quantitative and statistical study of the dynamics of clathrin-dependent and -independent endocytosis reveal a differential role of endophilinA2. *Cell Reports* **22**:1574–1588. DOI: https://doi.org/10.1016/j.celrep.2018.01.039, PMID: 29425511

Boutté Y, Jaillais Y. 2020. Metabolic cellular communications: feedback mechanisms between membrane lipid homeostasis and plant development. *Developmental Cell* **54**:171–182. DOI: https://doi.org/10.1016/j.devcel.2020.05.005, PMID: 32502395

Bücherl CA, Jarsch IK, Schudoma C, Segonzac C, Mbengue M, Robatzek S, MacLean D, Ott T, Zipfel C. 2017. Plant immune and growth receptors share common signalling components but localize to distinct plasma membrane nanodomains. *eLife* **6**:e25114. DOI: https://doi.org/10.7554/eLife.25114, PMID: 28262094

Cao Y, Aceti DJ, Sabat G, Song J, Makino S, Fox BG, Bent AF. 2013. Mutations in FLS2 Ser-938 dissect signaling activation in FLS2-mediated Arabidopsis immunity. *PLOS Pathogens* **9**:e1003313. DOI: https://doi.org/10.1371/journal.ppat.1003313, PMID: 23637603

Chen Y, Munteanu AC, Huang YF, Phillips J, Zhu Z, Mavros M, Tan W. 2009. Mapping receptor density on live cells by using fluorescence correlation spectroscopy. *Chemistry* **15**:5327-36. DOI: https://doi.org/10.1002/chem.200802305, PMID: 19360825

Chi Y, Wang C, Wang M, Wan D, Huang F, Jiang Z, Crawford BM, Vo-Dinh T, Yuan F, Wu F, Pei ZM. 2021. Flg22-induced $Ca^{2+}$ increases undergo desensitization and resensitization. *Plant, Cell & Environment* **44**:3563-3575. DOI: 10.1111/pce.14186, PMID: 34536020.

Chinchilla D, Bauer Z, Regenass M, Boller T, Felix G. 2006. The Arabidopsis receptor kinase FLS2 binds flg22 and determines the specificity of flagellin perception. *Plant Cell* **18**:465-476. DOI: https://doi.org/10.1105/tpc.105.036574, PMID: 16377758

Chinchilla D, Zipfel C, Robatzek S, Kemmerling B, Nürnberger T, Jones JD, Felix G, Boller T. 2007. A flagellin-induced complex of the receptor FLS2 and BAK1 initiates plant defence. *Nature* **448**:497-500. DOI: https://doi.org/10.1038/nature05999, PMID: 17625569

Cui Y, Li X, Yu M, Li R, Fan L, Zhu Y, Lin J. 2018. Sterols regulate endocytic pathways during flg22-induced defense responses in Arabidopsis. *Development* **145**: dev165688. DOI: https://doi.org/10.1242/dev.165688, PMID: 30228101

Ding LN, Li YT, Wu YZ, Li T, Geng R, Cao J, Zhang W, Tan XL. 2022. Plant disease resistance-related signaling pathways: Recent progress and future prospects. *International Journal of Molecular Sciences* **23**:16200. DOI: https://doi.org/10.3390/ijms232416200, PMID: 36555841

Dorrity MW, Saunders LM, Queitsch C, Fields S, Trapnell C. 2020. Dimensionality reduction by UMAP to visualize physical and genetic interactions. *Nature Communications* **11**:1537. DOI: https://doi.org/10.1038/s41467-020-15351-4, PMID: 32210240

Geng X, Ge B, Liu Y, Wang X, Dong K, Zhang Y, Chen Y, Lu C. 2022. Genome-wide identification and functional analysis of silicon transporter family genes in moso bamboo (Phyllostachys edulis). *International Journal of Biological Macromolecules* **223**:1705-1719. DOI: https://doi.org/10.1016/j.ijbiomac.2022.10.099, PMID: 36252629

Greig J, Bulgakova NA. 2021. Fluorescence recovery after photobleaching to study the dynamics of membrane-bound proteins *in vivo* using the Drosophila embryo. *Methods in Molecular Biology* **2179**:145–159. DOI: https://doi.org/10.1007/978-1-0716-0779-4_13, PMID: 32939719

Gronnier J, Franck CM, Stegmann M, DeFalco TA, Abarca A, von Arx M, Dünser K, Lin W, Yang Z, Kleine-Vehn J, Ringli C, Zipfel C. 2022. Regulation of immune receptor kinase plasma membrane nanoscale organization by a plant peptide hormone and its receptors. *eLife* **11**:e74162. DOI: https://doi.org/10.7554/eLife.74162, PMID: 34989334

Heese A, Hann DR, Gimenez-Ibanez S, Jones AM, He K, Li J, Schroeder JI, Peck SC, Rathjen JP. 2007. The receptor-like kinase SERK3/BAK1 is a central regulator of innate immunity

in plants. *Proceedings of the National Academy of Sciences of the United States of America* **104**:12217-22. DOI: https://doi.org/10.1073/pnas.0705306104, PMID: 17626179

Huang D, Sun Y, Ma Z, Ke M, Cui Y, Chen Z, Chen C, Ji C, Tran TM, Yang L, Lam SM, Han Y, Shu G, Friml J, Miao Y, Jiang L, Chen X. 2019. Salicylic acid-mediated plasmodesmal closure via Remorin-dependent lipid organization. *Proceedings of the National Academy of Sciences of the United States of America* **116**:21274-21284. DOI: https://doi.org/10.1073/pnas.1911892116, PMID: 31575745

Hudson A, Mullens A, Hind S, Jamann T, Balint-Kurti P. 2024. Natural variation in the pattern-triggered immunity response in plants: Investigations, implications and applications. *Molecular Plant Pathology* **25**:e13445. DOI: https://doi.org/10.1111/mpp.13445, PMID: 38528659

Jiao C, Gong J, Guo Z, Li S, Zuo Y, Shen Y. 2022. Linalool activates oxidative and calcium burst and CAM3-ACA8 participates in calcium recovery in Arabidopsis leaves. *International Journal of Molecular Sciences*, **23**: 5357. DOI: https://doi.org/10.3390/ijms23105357, PMID: 35628166

Kaiserli E, Sullivan S, Jones MA, Feeney KA, Christie JM. 2009. Domain swapping to assess the mechanistic basis of Arabidopsis phototropin 1 receptor kinase activation and endocytosis by blue light. *Plant Cell* **21**:3226-3244. DOI: https://doi.org/10.1105/tpc.109.067876, PMID: 19880798

Kontaxi C, Kim N, Cousin MA. 2023. The phospho-regulated amphiphysin/endophilin interaction is required for synaptic vesicle endocytosis. *Journal of Neurochemistry* **166**:248–264. DOI: https://doi.org/10.1111/jnc.15848, PMID: 37243578

Lee Y, Phelps C, Huang T, Mostofian B, Wu L, Zhang Y, Tao K, Chang YH, Stork PJ, Gray JW, Zuckerman DM, Nan X. 2019. High-throughput, single-particle tracking reveals nested membrane domains that dictate KRasG12D diffusion and trafficking. *eLife* **8**:e46393. DOI: https://doi.org/10.7554/eLife.46393, PMID: 31674905

Leslie ME, Heese A. 2017. Quantitative analysis of ligand-induced endocytosis of FLAGELLIN-SENSING 2 using automated image segmentation. *Methods in Molecular Biology* **1578**:39–54. DOI: https://doi.org/10.1007/978-1-4939-6859-6_4, PMID: 28220414

Levet F, Hosy E, Kechkar A, Butler C, Beghin A, Choquet D, Sibarita JB. 2015. SR-Tesseler: a method to segment and quantify localization-based super-resolution microscopy data. *Nature Methods* **12**:1065-71. DOI: https://doi.org/10.1038/nmeth.3579, PMID: 26344046

Liang X, Zhou JM. 2018. Receptor-like cytoplasmic kinases: Central players in plant receptor kinase-mediated signaling. *Annual Review of Plant Biology* **69**:267-299. DOI: https://doi.org/10.1146/annurev-arplant-042817-040540, PMID: 29719165

Li B, Meng X, Shan L, He P. 2016. Transcriptional regulation of pattern-triggered immunity in plants. *Cell Host Microbe* **19**:641-50. DOI: https://doi.org/10.1016/j.chom.2016.04.011, PMID: 27173932

Li M, Ong CY, Langouët-Astrié CJ, Tan L, Verma A, Yang Y, Zhang X, Shah DK, Schmidt EP, Xu D. 2022. Heparan sulfate-dependent RAGE oligomerization is indispensable for pathophysiological functions of RAGE. *eLife* **11**:e71403. DOI: https://doi.org/10.7554/eLife.71403, PMID: 35137686

Loiseau J, Robatzek S. 2017. Detection and analyses of endocytosis of plant receptor kinases.

*Methods in Molecular Biology* **1621**:177–189. DOI: https://doi.org/10.1007/978-1-4939-7063-6_17, PMID: 28567654

Lu D, Wu S, Gao X, Zhang Y, Shan L, He P. 2010. A receptor-like cytoplasmic kinase, BIK1, associates with a flagellin receptor complex to initiate plant innate immunity. *Proceedings of the National Academy of Sciences of the United States of America* **107**:496-501. DOI: https://doi.org/10.1073/pnas.0909705107, PMID: 20018686

Lv X, Jing Y, Xiao J, Zhang Y, Zhu Y, Julian R, Lin J. 2017. Membrane microdomains and the cytoskeleton constrain AtHIR1 dynamics and facilitate the formation of an AtHIR1-associated immune complex. *Plant Journal* **90**:3-16. DOI: https://doi.org/10.1111/tpj.13480, PMID: 28081290

Macho AP, Zipfel C. 2014. Plant PRRs and the activation of innate immune signaling. *Molecular Cell* **54**:263-72. DOI: https://doi.org/10.1016/j.molcel.2014.03.028, PMID: 24766890

Martinière A, Zelazny E. 2021. Membrane nanodomains and transport functions in plant. *Plant Physiology* **187**:1839–1855. DOI: https://doi.org/10.1093/plphys/kiab312, PMID: 35235669

Ngou BPM, Jones JDG, Ding P. 2022. Plant immune networks. *Trends in Plant Science* **27**:255-273. DOI: https://doi.org/10.1016/j.tplants.2021.08.012, PMID: 34548213

Offringa R, Huang F. 2013. Phosphorylation-dependent trafficking of plasma membrane proteins in animal and plant cells. *Journal of Integrative Plant Biology* **55**:789–808. DOI: https://doi.org/10.1111/jipb.12096, PMID: 23945267

Orosa B, Yates G, Verma V, Srivastava AK, Srivastava M, Campanaro A, De Vega D, Fernandes A, Zhang C, Lee J, Bennett MJ, Sadanandom A. 2018. SUMO conjugation to the pattern recognition receptor FLS2 triggers intracellular signalling in plant innate immunity. *Nature Communications* **9**: 5185. DOI: https://doi.org/10.1038/s41467-018-07696-8, PMID: 30518761

Robatzek S, Chinchilla D, Boller T. 2006. Ligand-induced endocytosis of the pattern recognition receptor FLS2 in Arabidopsis. *Genes Development* **20**:537–542. DOI: https://doi.org/10.1101/gad.366506, PMID: 16510871

Sanguankiattichai N, Buscaill P, Preston GM. 2022. How bacteria overcome flagellin pattern recognition in plants. *Current Opinion in Plant Biology* **67**:102224. DOI: https://doi.org/10.1016/j.pbi.2022.102224, PMID: 35533494

Su B, Wang A, Xie D, Shan X. 2023. VA-TIRFM-based SM kymograph analysis for dwell time and colocalization of plasma membrane protein in plant cells. *Plant Methods* **19**:70. DOI: https://doi.org/10.1186/s13007-023-01047-5, PMID: 37422677

Su B, Zhang X, Li L, Abbas S, Yu M, Cui Y, Baluška F, Hwang I, Shan X, Lin J. 2021. Dynamic spatial reorganization of BSK1 complexes in the plasma membrane underpins signal-specific activation for growth and immunity. *Molecular Plant* **14**:588–603. DOI: https://doi.org/10.1016/j.molp.2021.01.019, PMID: 33524551

Sun Y, Li L, Macho AP, Han Z, Hu Z, Zipfel C, Zhou JM, Chai J. 2013. Structural basis for flg22-induced activation of the Arabidopsis FLS2-BAK1 immune complex. *Science* **342**:624-628. DOI: https://doi.org/10.1126/science.1243825, PMID: 24114786

Vitrac H, Mallampalli VKPS, Dowhan W. 2019. Importance of phosphorylation/dephosphorylation cycles on lipid-dependent modulation of membrane

protein topology by posttranslational phosphorylation. *Journal of Biological Chemistry* **294**:18853–18862. DOI: https://doi.org/10.1074/jbc.RA119.010785, PMID: 31645436

Wang L, Li H, Lv X, Chen T, Li R, Xue Y, Jiang J, Jin B, Baluška F, Šamaj J, Wang X, Lin J. 2015. Spatiotemporal dynamics of the BRI1 receptor and its regulation by membrane microdomains in living Arabidopsis cells. *Molecular Plant* **8**:1334-49. DOI: https://doi.org/10.1016/j.molp.2015.04.005, PMID: 25896454

Xing J, Ji D, Duan Z, Chen T, Luo X. 2022. Spatiotemporal dynamics of FERONIA reveal alternative endocytic pathways in response to flg22 elicitor stimuli. *New Phytologist* **235**:518-532. DOI: https://doi.org/10.1111/nph.18127, PMID: 35358335

Xue Y, Xing J, Wan Y, Lv X, Fan L, Zhang Y, Song K, Wang L, Wang X, Deng X, Baluška F, Christie JM, Lin J. 2018. Arabidopsis blue light receptor phototropin 1 undergoes blue light-induced activation in membrane microdomains. *Molecular Plant* **11**:846-859. DOI: https://doi.org/10.1016/j.molp.2018.04.003, PMID: 29689384

Zhang J, Li W, Xiang T, Liu Z, Laluk K, Ding X, Zou Y, Gao M, Zhang X, Chen S, Mengiste T, Zhang Y, Zhou JM. 2010. Receptor-like cytoplasmic kinases integrate signaling from multiple plant immune receptors and are targeted by a Pseudomonas syringae effector. *Cell Host Microbe* **7**:290-301. DOI: https://doi.org/10.1016/j.chom.2010.03.007, PMID: 20413097

Zhang X, Cui Y, Yu M, Su B, Gong W, Baluška F, Komis G, Šamaj J, Shan X, Lin J. 2019. Phosphorylation-mediated dynamics of nitrate transceptor NRT1.1 regulate auxin flux and nitrate signaling in lateral root growth. *Plant Physiology* **181**:480–498. DOI: https://doi.org/10.1104/pp.19.00346, PMID: 31431511

Zhong YH, Guo ZJ, Wei MY, Wang JC, Song SW, Chi BJ, Zhang YC, Liu JW, Li J, Zhu XY, Tang HC, Song LY, Xu CQ, Zheng HL. 2023. Hydrogen sulfide upregulates the alternative respiratory pathway in mangrove plant Avicennia marina to attenuate waterlogging-induced oxidative stress and mitochondrial damage in a calcium-dependent manner. *Plant Cell and Environment* **46**:1521-1539. DOI: https://doi.org/10.1111/pce.14546, PMID: 36658747

Zhou R, Liu H, Ju T, Dixit R. 2020. Quantifying the polymerization dynamics of plant cortical microtubules using kymograph analysis. *Methods in Cell Biology* **160**:281–293. DOI: https://doi.org/10.1016/bs.mcb.2020.04.006, PMID: 3289

Zinchuk V, Wu Y, Grossenbacher-Zinchuk O, Stefani E. 2011. Quantifying spatial correlations of fluorescent markers using enhanced background reduction with protein proximity index and correlation coefficient estimations. *Nature Protocols* **6**:1554-67. DOI: 10.1038/nprot.2011.384, PMID: 21959238

Zipfel C, Robatzek S, Navarro L, Oakeley EJ, Jones JD, Felix G, Boller T. 2004. Bacterial disease resistance in Arabidopsis through flagellin perception. *Nature* **428**:764-7. DOI: https://doi.org/10.1038/nature02485, PMID: 15085136

## Figures and Figure legends

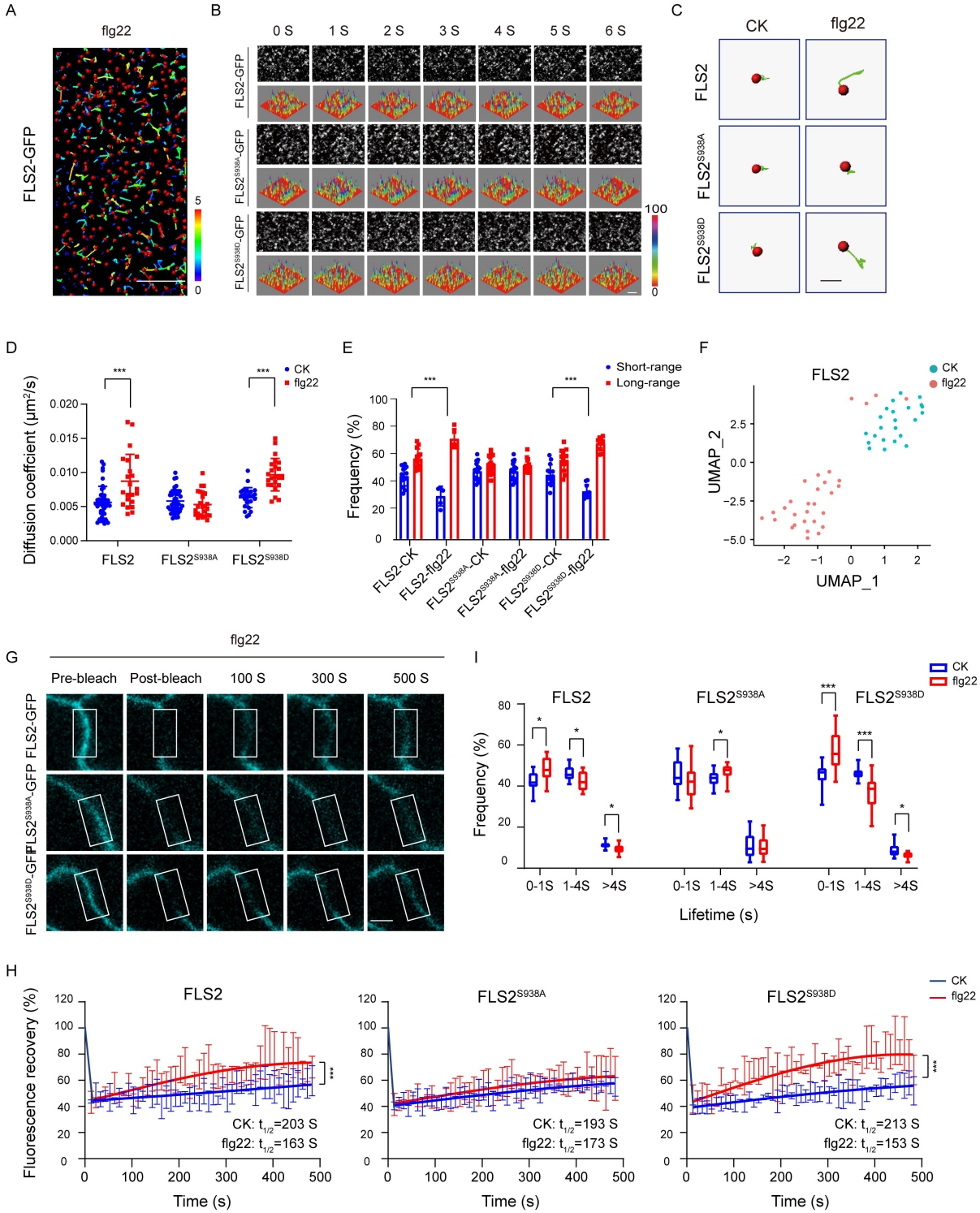


**Figure 1. Effects of Ser-938 phosphorylation on the spatiotemporal dynamics of FLS2 at the plasma membrane.**

**(A)** VA-TIRFM images of a FLS2-expressing hypocotyl cell was analyzed. The

5-day-old transgenic Arabidopsis plant cells were observed under VA-TIRFM. The red balls indicate the positions of the identified points that appeared. Trajectories represent the track length of the identified points. Bar = 10μm. (**B**) Time-lapse images of FLS2, FLS2$^{S938A}$, and FLS2$^{S938D}$. Bar = 2 μm. The fluorescence intensity changes among different 3D luminance plots. (**C**) The trajectories of representative individual FLS2, FLS2$^{S938A}$ and FLS2$^{S938D}$ under 30 min for 10 μM flg22 processing and control. Bar = 0.5 μm. (**D**) Diffusion coefficients of FLS2 (control, n = 42 spots; flg22, n = 24 spots), FLS2$^{S938A}$ (control, n = 44 spots; flg22, n = 25 spots) and FLS2$^{S938D}$ (control, n = 27 spots; flg22, n = 23 spots) under different environments. Statistical significance was assessed with the Student's *t*-test (***$p < 0.001$). Error bars represent the SD. (**E**) Frequency of long- and short-range motions for FLS2 (control, n = 15 spots; flg22, n = 5 spots), FLS2$^{S938A}$ (control, n = 16 spots; flg22, n = 14 spots), and FLS2$^{S938D}$ (control, n = 14 spots; flg22, n = 13 spots) under different environments. Statistical significance was assessed with the Student's *t*-test (***$p < 0.001$). Error bars represent the SD. (**F**) UMAP visualization of FLS2 samples under different conditions (control, n = 25 spots; flg22, n = 22 spots). Dots represent the individual images, and are colored according to the reaction conditions. (**G**) The representative FRAP time course of FLS2-GFP, FLS2$^{S938A}$, and FLS2$^{S938D}$ under flg22 treatments. White squares indicate bleached regions. Bar = 5 μm. (**H**) Fluorescence recovery curves of the photobleached areas with or without the flg22 treatment. Three biological replicates were performed. Each experiment was repeated thrice independently (n = 3 images). Statistical significance was assessed with the Student's *t*-test (***$p < 0.001$). Error bars represent the SD. (**I**) lifetime were analyzed for FLS2 (control, n = 13 spots; flg22, n = 9 spots), FLS2$^{S938A}$ (control, n = 28 spots; flg22, n = 21 spots), and FLS2$^{S938D}$ (control, n = 13 spots; flg22, n = 15 spots) under the control and flg22 treatments. The data points were collected from a TIRFM time series using an exposure time of 100ms to capture a total duration of 20 s. Statistical significance was assessed with the Student's *t*-test (*$p < 0.05$, ***$p <$

0.001). Error bars represent the SD.

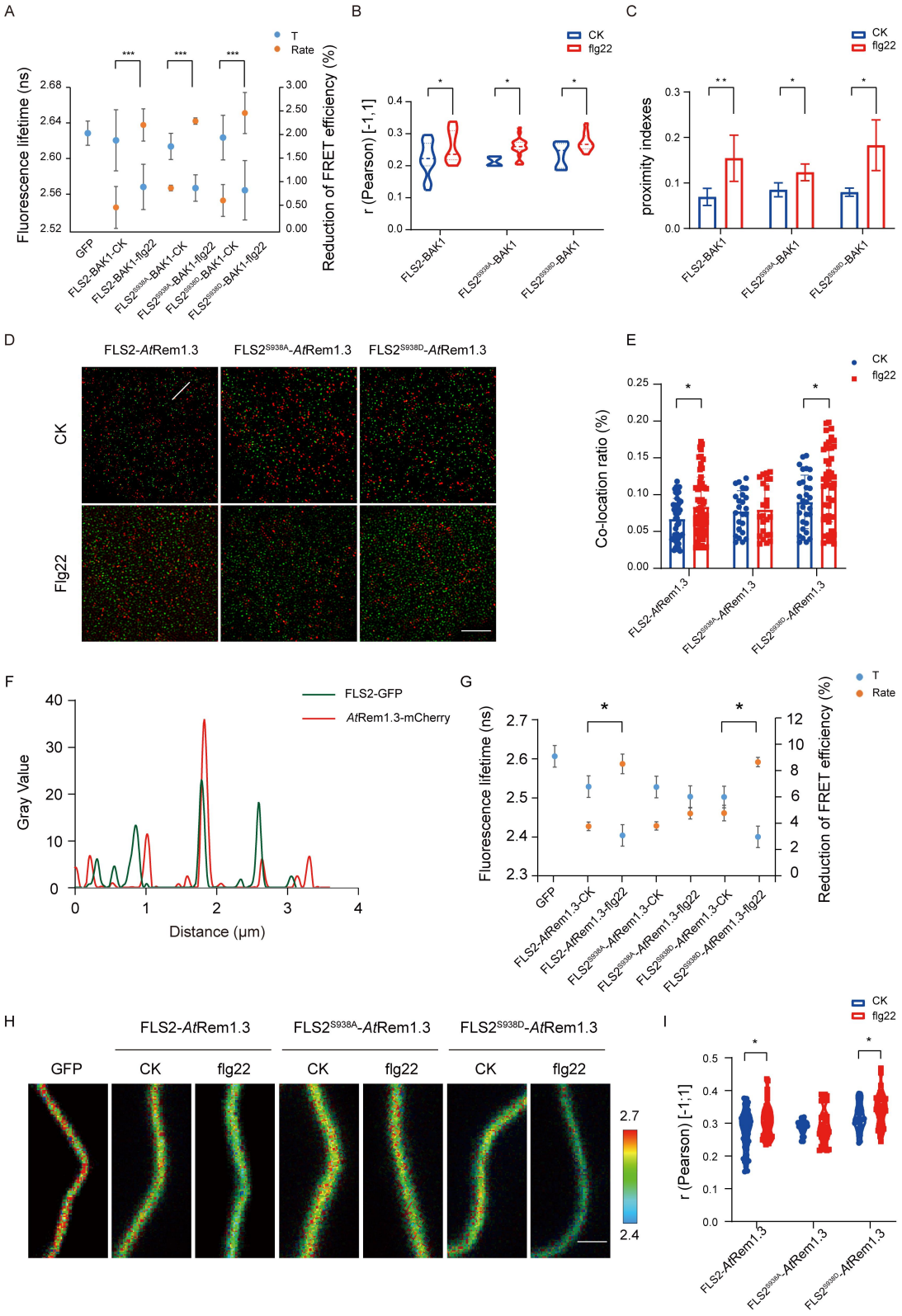


**Figure 2. Different Ser-938 phosphorylation states of FLS2 affect its partitioning into *At*Rem1.3-associated nanodomains.**

(**A**) FLIM-FRET was used to detect the co-expression of FLS2/FLS2$^{S938A}$/FLS2$^{S938D}$-GFP and BAK1-mCherry in the *N. benthamiana* epidermal cells stimulated by 1/2 MS or flg22 (10 μM) for 30 min. Average fluorescence lifetime (*t*) and the FRET efficiency were analyzed for FLS2 (control, n = 22 images; flg22, n= 15 images), FLS2$^{S938A}$ (control, n = 19 images; flg22, n= 12 images), or FLS2$^{S938D}$ (control, n = 24 images; flg22, n= 15 images) and BAK1. The fluorescence mean lifetime (T) of FLS2-GFP (n = 8 images). Statistical significance was assessed with the Student's *t*-test (***$p < 0.001$). Error bars represent the SD. (**B**) Pearson correlation coefficient values of co-localization between FLS2 (control, n = 24 images; flg22, n= 15 images), FLS2$^{S938A}$ (control, n = 18 images; flg22, n= 22 images), or FLS2$^{S938D}$ (control, n = 15 images; flg22, n= 20 images) and BAK1 upon stimulation with control or flg22. Statistical significance was assessed with the Student's *t*-test (*$p < 0.05$). Error bars represent the SD. (**C**) Mean protein proximity indexes showing FLS2 (control, n = 8 images; flg22, n= 5 images), FLS2$^{S938A}$ (control, n = 4 images; flg22, n= 3 images) or FLS2$^{S938D}$ (control, n = 4 images; flg22, n= 3 images) and BAK1 degree of proximity under different conditions. Statistical significance was assessed with the Student's *t*-test (*$p < 0.05$; **$p < 0.01$). Error bars represent the SD. (**D**) TIRF-SIM images of the Arabidopsis leaf epidermal cells co-expressing FLS2/FLS2$^{S938A}$/FLS2$^{S938D}$-GFP and *At*Rem1.3-mCherry under different environments. The distribution of FLS2 and *At*Rem1.3 signals along the white line in the merged image. Bar = 5 μm. (**E**) The histogram shows the co-localization ratio of FLS2-GFP (control, n = 52 images; flg22, n= 61 images), FLS2$^{S938A}$-GFP (control, n = 30 images; flg22, n= 36 images) or FLS2$^{S938D}$-GFP (control, n = 34 images; flg22, n= 54 images) and *At*Rem1.3-mCherry. The sizes of the ROIs used for statistical analysis are 13.38 μm and 13.38 μm. Statistical significance was assessed with the Student's *t*-test (*$p < 0.05$). Error bars represent the SD. (**F**) FLS2/FLS2$^{S938A}$/FLS2$^{S938D}$-GFP and *At*Rem1.3-mCherry fluorescence signals as shown in D. (**G**) The fluorescence mean lifetime (T) and the corrected

fluorescence resonance efficiency (Rate) of FLS2 (control, n = 8 images; flg22, n= 13 images), FLS2$^{S938A}$ (control, n = 9 images; flg22, n= 11 images), or FLS2$^{S938D}$ (control, n = 10 images; flg22, n= 11 images) with co-expressed *At*Rem1.3. The fluorescence mean lifetime (T) of FLS2-GFP (n = 9 images). Statistical significance was assessed with the Student's *t*-test (***$p < 0.001$). Error bars represent the SD. (**H**) Intensity and lifetime maps of the Arabidopsis leaf epidermal cells co-expressing FLS2/FLS2$^{S938A}$/FLS2$^{S938D}$-GFP and *At*Rem1.3-mCherry as measured by FLIM-FRET. Bar = 2 μm. (**I**) Quantification of co-localization between FLS2, FLS2$^{S938A}$ or FLS2$^{S938D}$ and *AtRem1.3* with and without stimulation with ligands. Pearson correlation coefficient values (*r*) were obtained between FLS2 (control, n = 66 images; flg22, n= 53 images) /FLS2$^{S938A}$ (control, n = 42 images; flg22, n= 54 images) /FLS2$^{S938D}$-GFP (control, n = 29 images; flg22, n= 38 images) and *At*Rem1.3-mCherry. Statistical significance was assessed with the Student's *t*-test (*$p < 0.05$). Error bars represent the SD.

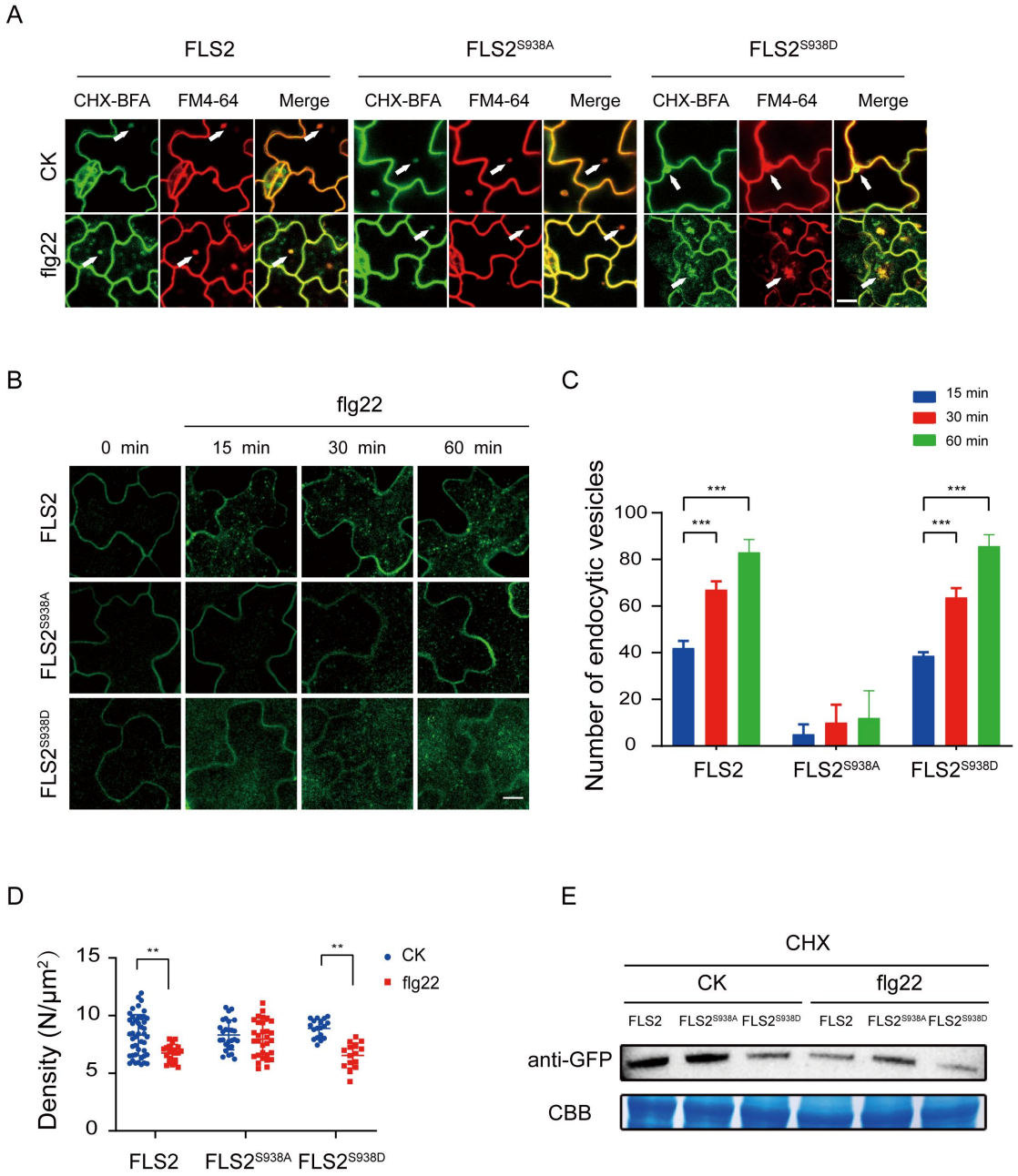


**Figure 3. The Ser-938 phosphorylation site affects flg22-induced endocytosis.**

**(A)** Confocal images of FLS2/FLS2$^{S938A}$/FLS2$^{S938D}$-GFP in *Arabidopsis thaliana* leaf epidermal cells. Firstly, experiments were performed after pretreatment with CHX (50 μM) for 30 min. Subsequently, to observe subcellular localization, FLS2/FLS2$^{S938A}$/FLS2$^{S938D}$-GFP were treated with 60 min of BFA (50 μM) and then exposed or not to flg22 (10 μM). Finally, the transgenic seedlings were stained with FM4-64 (5 μM, 30 min). White arrows

indicate BFA bodies. Bar = 3μm. (**B**) Images of FLS2/FLS2$^{S938A}$/FLS2$^{S938D}$-GFP in *Arabidopsis thaliana* leaf epidermal cells treated with 10 μM flg22 for 15, 30, and 60 min. Bar = 3μm. (**C**) Analysis of FLS2 (15 min, n = 4 images; 30 min, n= 4 images; 60 min, n= 4 images), FLS2$^{S938A}$ (15 min, n = 5 images; 30 min, n= 5 images; 60 min, n= 5 images), and FLS2$^{S938D}$ (15 min, n = 5 images; 30 min, n= 5 images; 60 min, n= 5 images) endocytic vesicle numbers in cells treated with 10 μM flg22 treatment over time. Statistical significance was assessed with the Student's *t*-test (***$p < 0.001$). Error bars represent the SD. (**D**) The signal density of FLS2 (control, n = 45 images; flg22, n= 24 images), FLS2$^{S938A}$ (control, n = 31 images; flg22, n= 34 images) and FLS2$^{S938D}$ (control, n = 18 images; flg22, n= 15 images) in cells after control or 10 μM flg22 treatments for 30 min as measured by FCS. Statistical significance was assessed with the Student's *t*-test (**$p < 0.01$). Error bars represent the SD. (**E**) Immunoblot analysis of FLS2 protein in 10-day-old transgenic Arabidopsis plant upon stimulation with or without 10 μM flg22. CBB, a loading control dyed with Coomassie Brilliant Blue.

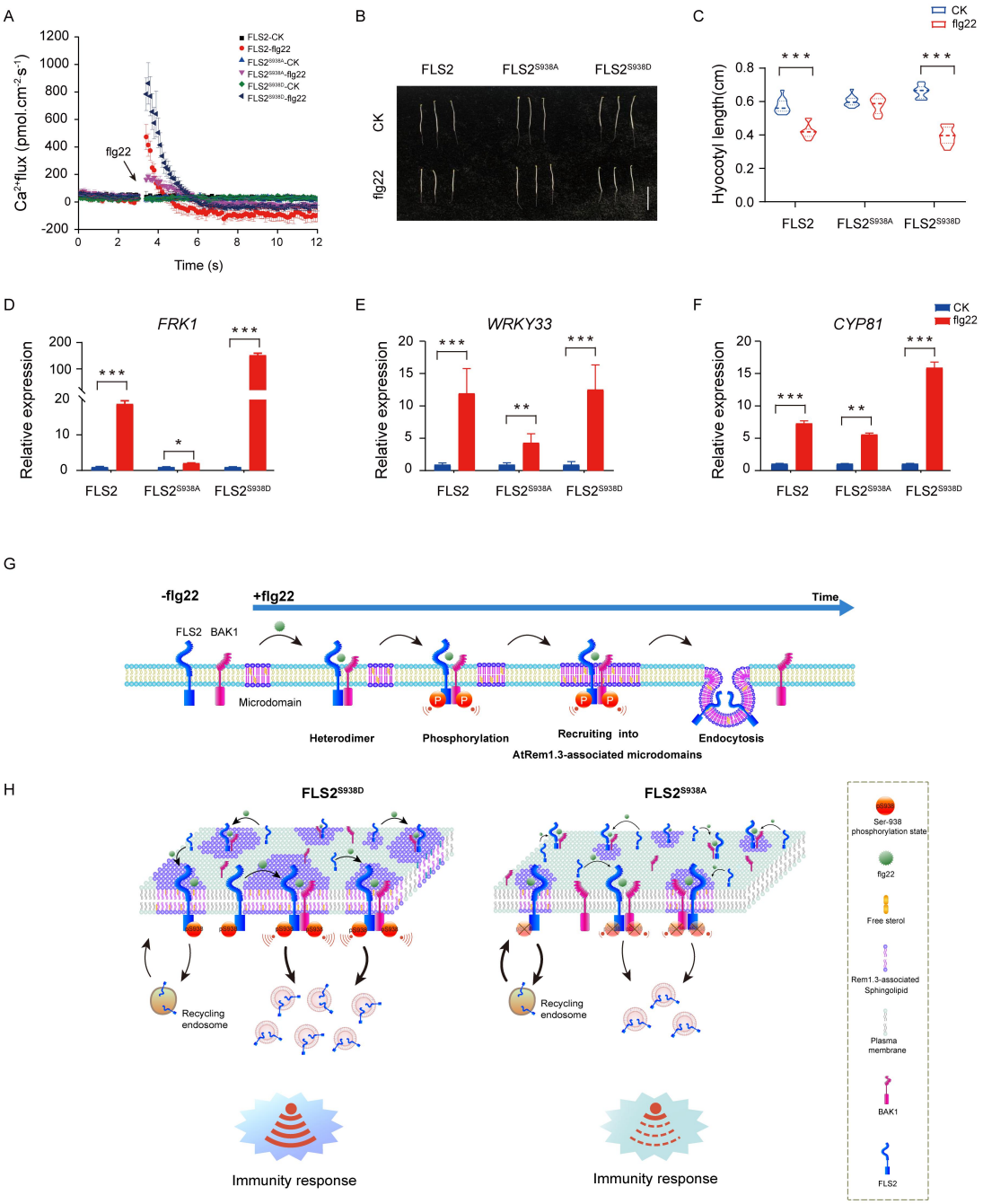


**Figure 4. Ser-938 phosphorylation is essential for various flg22-induced PTI responses.**

**(A)** The flg22-induced transient $Ca^{2+}$ flux in 20-day-old transgenic leaf cells. The $Ca^{2+}$ flux was continuously recorded for 12 min in the test medium. Each point represents the average value for about 12 individual plants ± SEM. (**B**) Phenotypes of 5-day old etiolated seedlings grown in the presence of 1/2 MS

(control) or 10 μM flg22 solid medium. Bar=0.5cm. (**C**) Hypocotyl length of FLS2 (control, n = 13 seedlings; flg22, n= 13 seedlings), $FLS2^{S938A}$ (control, n = 13 seedlings; flg22, n= 13 seedlings) and $FLS2^{S938D}$ (control, n = 13 seedlings; flg22, n= 13 seedlings) transgenic plants. Statistical significance was assessed with the Student's *t*-test (***$p < 0.001$). Error bars represent the SD. (**D-F**) mRNA levels of the PTI marker genes FRK1/WRKY33/CYP81 were significantly different between the FLS2, $FLS2^{S938A}$, and $FLS2^{S938D}$ 10-day-old transgenic Arabidopsis plant after treatment with 10 μM flg22 for 30 min. Total RNA was extracted from 10-day-old seedlings and analyzed using qRT-PCR, with transcript levels being normalized to *UBQ5*. Three biological replicates were performed. Each experiment was repeated thrice independently (n = 3). Statistical significance was assessed with the Student's *t*-test (*$p < 0.5$, **$p < 0.01$, ***$p < 0.001$). Error bars represent SD. (**G**) The working model for the spatiotemporal dynamic regulation of FLS2 phosphorylation at the plasma membrane upon flg22 stimulation. (**H**) Dynamic model of FLS2 with different Ser-938 phosphorylation states upon stimulation with flg22.